A Low-Power MCU-Based MPPT Architecture With a Fast Impedance Measurement for Broadband Piezoelectric Energy Harvesting

Nicolas Decroix, Pierre Gasnier, Adrien Morel, David Gibus, and Adrien Badel

***Abstract*—This article presents the combination of a fast and robust maximum power point tracking algorithm called two-load characterization method (TLCM) and an efficient energy harvesting interface called resistive short circuit (RSC) for broadband piezoelectric energy harvesting. The proposed architecture is implemented using a low-power microcontroller (STM32L4) with its associated discrete electronics. The TLCM consists of an embedded impedance measurement that computes the piezoelectric impedance after two successive phase and voltage measurements. It calculates the optimal load impedance as the complex conjugate of the generator output impedance. It is up to 13 times faster than classical Perturbation and Observation algorithms. The complex conjugate impedance is then emulated by the RSC interface: a Flyback converter emulates a resistive load while a variable duration short-circuit following the zero voltage instant emulates a capacitive load. This two-parameters electrical interface allows a 9.4% harvested power bandwidth, which is 35% more than for a fixed resistor. The whole system is tested at 0.5 m/s^2 peak ambient acceleration and between 26 Hz to 30 Hz in standalone operation. In those conditions, the proposed system showed an end-to-end efficiency in the 65% to 80% range while consuming 21.5 μW to 28.5 μW, with a measurement duty cycle of 13%. It harvests a net maximum power of 157 μW with a peak extracted power of 235 μW.**

***Index Terms*—Complex impedance matching, electrical interface, maximum power point tracking, microcontroller, piezoelectric vibration energy harvesting, power management circuit.**

I. Introduction

VIBRATIONAL energy harvesting has emerged as a promising technology for powering small electronic devices [1]. Indeed, in harsh or closed environments near vibration sources, scavenging vibration becomes a relevant alternative when batteries cannot be used [2]. However, efficiently converting this ambient energy into usable electrical power remains a significant challenge due to the unpredictable and varying nature of ambient vibrations. Piezoelectric transduction, as opposed to electromagnetic or electrostatic transductions, offers the benefit of producing voltages ranges that are suitable for associated electronics (2 V–20 V), along with a relatively high power density even at small scales [3], [4]. Piezoelectric energy harvesters (PEH) generally rely on cantilever-type structures to amplify input vibrations through a mechanical resonator. One major challenge with this structure is the frequency mismatch between the ambient vibration and the resonator's natural frequency. To address this limitation, it is crucial to operate the PEH at its maximum power point (MPP) by achieving impedance matching over a wide frequency band [5], to ensure optimal power extraction from the harvester.

Several solutions to enlarge the power bandwidth have been proposed in the state of the art. Mechanical systems that incorporate multiple resonant frequencies have been used; however, their power densities are often very low [6]. Nonlinear systems are also a promising solution, but their intricate dynamics and the presence of multiple coexisting orbits require the use of orbit control systems, which are energy hungry [7], [8]. Finally, systems that tune the resonant frequency by adapting the harvester's stiffness to align with the ambient frequency show great promise. To change this stiffness, some researches focused on mechanical tuning [9] by using small actuators at the expense of power density. It is also possible to use piezoelectric tuning [10], [11] by using two piezoelectric patches on a single harvester, one for the tuning and the other for harvesting energy but it often needs high actuation voltages (>100 V). Electrical tuning approaches, on the contrary, do not require large volume, energy, nor voltage to tune the resonant frequency of PEH on large frequency range, and can be implemented with self-powered circuits [10], [12]. In this case, the electrical circuit has a significant impact on the mechanical dynamics of the system [13], [14], [15]. To that end, researches have been carried out to increase the coupling coefficient k_m^2 of PEH [12], [16], [17], to maximize the impact of electrical interfaces on the harvester's bandwidth. Indeed, it has been demonstrated that using low power electronics and efficient electrical interfaces can extend the frequency bandwidth by up to 36% [16]. The operation principle of such a solution is based on two distinct but interdependent parts: the electrical interface and the maximum power point tracking (MPPT) algorithms, which are both described as follows.

Manuscript received 8 April 2024; revised 24 June 2024; accepted 17 July 2024. Date of publication 29 July 2024; date of current version 11 September 2024. Recommended for publication by Associate Editor B. Shao. *(Corresponding author: Nicolas Decroix)*

Nicolas Decroix is with the Université Grenoble Alpes, CEA, Leti, F-38000 Grenoble, France, and also with the Université Savoie Mont Blanc, SYMME, 74000 Annecy, France (e-mail: nicolas.decroix@univ-smb.fr).

Pierre Gasnier is with the Université Grenoble Alpes, CEA, Leti, F-38000 Grenoble, France (e-mail: pierre.gasnier@cea.fr).

Adrien Morel, David Gibus, and Adrien Badel are with the Université Savoie Mont Blanc, SYMME, 74000 Annecy, France (e-mail: adrien.morel@univ-smb.fr; david.gibus@univ-smb.fr; adrien.badel@univ-smb.fr).

Color versions of one or more figures in this article are available at https://doi.org/10.1109/TPEL.2024.3434548.

Digital Object Identifier 10.1109/TPEL.2024.3434548

Tunable electrical interfaces are required in order to harvest energy over a wide frequency bandwidth. In the case of highly-coupled PEHs, it can be shown that the internal impedance of the harvester is predominantly resistive and capacitive overall, except between the short and open-circuit resonant frequencies (f_{SC} and f_{OC}, respectively) where it becomes resistive and inductive. This is reminded in Sections II-A and II-B. Electrical interfaces based on nonlinear voltage treatments such as FTSECE [18] or SCSECE [19] were proposed for capacitive and inductive impedance matching, leading to the highest power envelopes in the state of the art [10]. However, those interfaces rely on the transfer of all the PEH energy on an inductor, which introduces resistive losses [18]. Even if it exhibits a slightly narrower bandwidth, the short-circuit (SC-)SEH interface [20] does not suffer from this problem as it relies on load emulation thank to a dc–dc converter working at a frequency higher than the mechanical frequency. In this case, electrical transients are very long due to the charging of a large intermediate storage capacitor. Moreover, it has been shown that these nonlinear interfaces can excite higher frequency modes of the PEH, which can lead to a decrease in the extracted power [16]. This effect can be largely mitigated with linear interfaces like the resistive capacitive (RC) interface [21], which does not excites higher modes and has a power bandwidth similar to the SC-SEH and the SCSECE. Nevertheless, to be implemented in a real system, the RC interface needs a bank of discrete capacitors [22] to cover the useful frequency bandwidth of the PEH.

Additionally, efficient and adaptive MPPT algorithms also need to be implemented [23] in order to harvest power for various conditions (frequency and acceleration). Indeed, the optimality conditions of the previously discussed electrical interfaces heavily depends on the input frequency. Lookup tables (LUT) algorithms [24] consist in storing optimal parameters of a given interface for several frequencies but are not robust against PEH parameters variations. Perturb and Observe (P&O) algorithms [25], [26], [27] frequently modify the tuning parameters to converge toward the maximum power point, but suffer from long convergence times. Discrete optimal couple tracking (DOCT) algorithms [28] consist in testing several couples of parameters and measuring the output power for each of them, the optimal couple being chosen afterward. Finally, impedance measurement has been used in [29], denoted as "calibration technique" to measure the output impedance of a given PEH to find the optimal parameters. The drawback here is that the PEH should be exempt from external vibration while making the measurement, a condition that cannot be realistically enforced in real-world scenarios.

Although previous research has provided valuable insights on efficient electrical interfaces or functional algorithms, there is still a need for an architecture that satisfy the robustness, and versatility criteria while providing a large power bandwidth. This article proposes to respond to this dual need with both a novel and efficient electrical interface and a high-performance, robust MPPT algorithm. The proposed algorithm is implemented with a microcontroller unit (MCU) with very low power consumption, which is an interesting and more flexible alternative to ASICs as well as being more accessible for low volumes production.

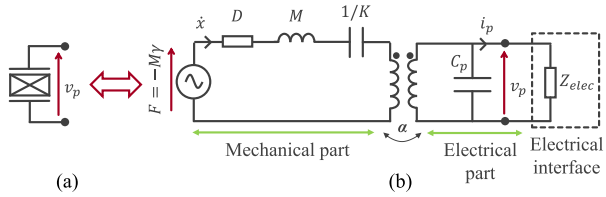

Fig. 1. (a) Symbol of the PEH and (b) complete circuit model of the PEH with its electrical interface.

The rest of this article is organized as follows. Section II provides elements about the modeling of PEH and the proposed two-load characterization method (TLCM) algorithm. In Section III, we detail the proposed resistive short circuit (RSC) interface. Section IV provides implementation and architectures. The experimental setup and results are presented in Section V. Discussion of the findings and a comparison to the state of art in Section VI. Finally, Section VII concludes this article.

II. Impedance Measurement Based MPPT Algorithm

A. PEH Modeling

As shown in Fig. 1, the PEH is modeled by a single degree of freedom linear mechanical resonator composed of an inertial mass M, a mechanical damper D, and a spring of stiffness K giving a mechanical resonator of quality factor $Q = \sqrt{KM}/D$ having a natural angular frequency $\omega_{SC} = 2\pi f_{sc} = \sqrt{K/M}$.

Piezoelectric coupling is taken into account by the electromechanical coupling term α, which leads to the well-known electromechanical model, extensively described in [10], [12], [23], and [30] and defined by

$$\begin{cases} F = -M\gamma = M\ddot{x} + D\dot{x} + Kx + \alpha v_p \\ i_p = \alpha\dot{x} - C_p\dot{v}_p. \end{cases} \tag{1}$$

The ambient acceleration γ is translated into a relative displacement x of the inertial mass with respect to the base. $k_m^2 = \alpha^2/KC_p$ is defined as the coupling coefficient of the PEH. The piezoelectric layer being strained, the resulting electrical charges are either stored in the piezoelectric material capacitance C_p or collected into an electrical interface whose input impedance is denoted Z_{elec} and which draws an electrical current i_p.

In this study, we assume that the impact of the dielectric losses is negligible, as well as the impact of the electrical interface on higher vibration modes of the PEH. Using the first-harmonic approximation [10], [23], which is known to be a reasonable assumption for high-Q factor resonators, the displacement of the resonator is assumed to remain sinusoidal ($x(t) = X_m \cos(\omega t)$), despite the nonsinusoidal shape of v_p.

The expression of the PEH internal impedance Z_{piezo} is given in (2), Ω being the normalized frequency ($\Omega = \omega/\omega_{SC}$). The expression of $\widetilde{Z_{piezo}}$, which corresponds to Z_{piezo} normalized by ωC_p, is also given in (3)

$$Z_{piezo} = \frac{1}{j\omega C_p}\left(\frac{1}{1+\frac{k_m^2}{1-\Omega^2+j\Omega/Q}}\right) \tag{2}$$

$$\widetilde{Z_{piezo}} = Z_{piezo}\,\omega C_p. \tag{3}$$

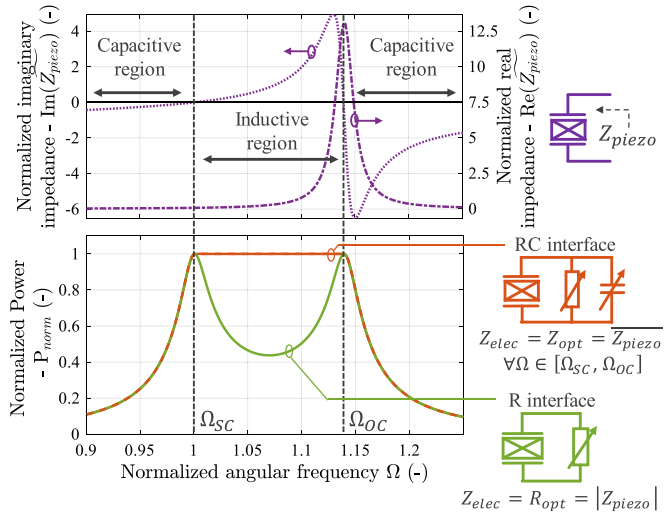

Fig. 2. Normalized imaginary part of the PEH impedance with normalized extracted power ($k_m^2 = 0.3$, $Q = 50$).

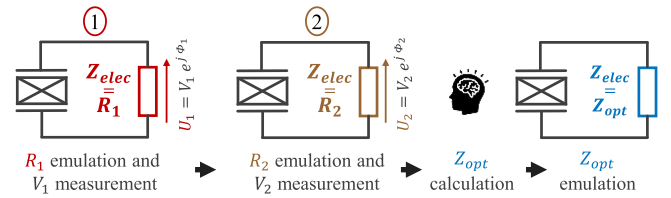

Fig. 3. $\boldsymbol{V}_{1,2}$ and $\boldsymbol{\Phi}_{1,2}$ measurement.

B. Optimal Impedance

To maximize the harvested power under any frequency in sinusoidal operation, the electrical interface impedance (Z_{elec}) must closely match the complex conjugate of the piezoelectric harvester's impedance (Z_{piezo}). For example, Fig. 2 shows the normalized real and imaginary part of the impedance $\widetilde{Z_{piezo}}$ as well as the electrical extracted power for an optimal RC interface ($Z_{elec} = R_{opt} \,//\, C_{opt}$) compared with an optimal resistive interface ($Z_{elec} = R_{opt}$) [21].

When working in real conditions, the impedance Z_{piezo} can vary because of external events like temperature variations or aging for example. Hence, there is a need for an algorithm that finds the optimal impedance (i.e., $\overline{Z_{piezo}}$, the complex conjugate of Z_{piezo}) and adapt the optimal parameters for a given electrical interface, enabling impedance matching for a wide bandwidth.

C. Proposed MPPT Algorithm: the TLCM

The proposed MPPT algorithm is based on a characterization method called the TLCM [31] proposed in a MPPT context, which relies on an embedded impedance measurement. As depicted in Fig. 3, the algorithm successively performs two types of measurements when connected to two different electrical loads R_1 and R_2: 1) measuring the phase difference (Φ_1, Φ_2) between the input acceleration and the PEH voltage (v_p), and 2) determining the PEH voltage amplitudes (V_1, V_2).

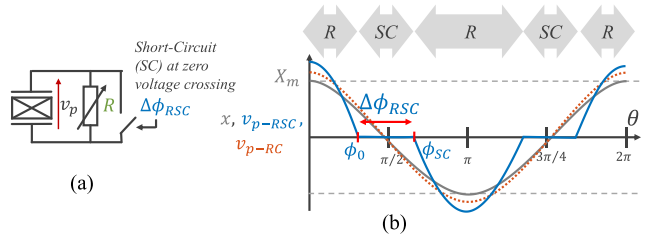

Fig. 4. (a) Operating principle and (b) ideal waveforms of the RSC interface showing the beam displacement (gray), the PEH voltage with RSC (blue), and the equivalent PEH voltage with RC (orange).

At the end of this measurement phase, the complex voltages $U_1 = V_1\ e^{j\ \Phi_1}$ and $U_2 = V_2\ e^{j\ \Phi_2}$ are determined. Consequently, the complex impedance of the generator Z_{piezo} is calculated thanks to (4), following the methodology outlined in [31]:

$$Z_{piezo} = \frac{(U_2 - U_1)\, R_1 R_2}{(U_1 R_2 - U_2 R_1)}. \tag{4}$$

At this stage, the system identifies the optimal impedance Z_{opt} to emulate, which is the complex conjugate of Z_{piezo}, as given in

$$Z_{elec} = Z_{opt} = \overline{Z_{piezo}}. \tag{5}$$

The selection of R_1 and R_2 should adhere to the recommendations in [31], suggesting resistance values should be on either side of $1/C_p\omega_{SC}$ in the absence of specific harvester knowledge. It is important to highlight that the energy harvesting process continues even during this measurement phase. It is, therefore, preferable that the measurement loads correspond approximately to the optimal impedance, Z_{opt}, to ensure optimal power extraction. Since resistive loads would lead to energy dissipation rather than harvesting, a practical implementation of this algorithm is discussed in Section IV. The following section details the emulation of Z_{opt} to efficiently extract electrical power from the PEH.

III. RSC Electrical Interface

A. Operation and Analytical Modeling of the RSC Interface

The proposed RSC interface is similar to the RC interface [21], [22] with the difference that a SC, whose duration is tunable, is performed at the zero PEH voltage instants instead of using a capacitor. When associated with the RSC interface, the PEH either operates in SC condition, or is connected to a resistive load. Fig. 4 depicts the operating principle and the ideal waveforms of the RSC interface as a function of the normalized angular frequency $\theta = \omega t$ with ϕ_0 the starting angle of the SC, ϕ_{sc} the ending angle of the SC and $\Delta\phi_{RSC} = \phi_{sc} - \phi_0$ the angular duration of the SC.

This SC advantageously induces a phase shift on the PEH voltage to emulate the imaginary part of Z_{opt} in order to compensate for the reactive part of Z_{piezo} between the SC (f_{SC}) and open-circuit (f_{OC}) frequencies. Other SC-based electrical interfaces emulating a capacitive behavior have already been proposed and are thoroughly detailed in [10] and [21]. Unlike

these latter electrical interfaces, the proposed RSC interface does not rely on a resonant transfer of all the energy from the piezoelectric capacitor to the load via an inductor. Instead, the energy is transferred in several steps, which reduces the size of the inductor and improves conversion efficiency. A dedicated and practical implementation of this electrical interface is described in Section IV. Fig. 4(b) also shows a comparison with the RC interface: for the same load and frequency, both interfaces can give the same power output because they emulate almost the same electrical damping and stiffness.

In order to express the average extracted power over a full mechanical period, the first harmonic expression of the output voltage is used (6), following the method described in [10], [18], and [30], which enables to identify the in-phase and out-of-phase parts of the PEH voltage, denoted ε_D and ε_K, respectively, as follows:

$$v_p = \frac{\alpha}{C_p}\, x\left(\varepsilon_K + j\varepsilon_D\right). \tag{6}$$

The expression of the normalized extracted power P_{norm} can, then, be expressed by (7) and the expression of the extracted power of the PEH by (8) (from [30])

$$P_{\text{norm}} = \frac{4k_m^2\varepsilon_D\frac{\Omega}{Q}}{\left(1-\Omega^2+k_m^2\varepsilon_K\right)^2+\left(\frac{\Omega}{Q}+k_m^2\varepsilon_D\right)^2} \tag{7}$$

$$P_{ext} = P_{\text{norm}}\, P_{\max} = P_{\text{norm}}\,\frac{\mathrm{M}^2\gamma^2}{8D}. \tag{8}$$

When connected to a resistive load, the expression of the PEH voltage v_p is found from Ohm's law, $i_p = v_p/R$, with R the resistive load connected the PEH. Solving the second differential equation of (1) in continuous sinusoidal operation, the PEH voltage is expressed over half a mechanical period by

$$\begin{cases} v_p(\theta) = -A\sin(\theta) + B\cos(\theta) + c(\theta),\ \forall\theta\in[\phi_0,\phi_{\text{sc}}] \\ v_p(\theta) = 0,\ \forall\theta\in[\phi_{\text{SC}},\phi_0+\Delta\phi_{\text{SC}}]. \end{cases} \tag{9}$$

With

$$\begin{cases} A = \frac{\alpha X_m}{C_p}\left[\frac{r\Omega}{1+(r\Omega)^2}\right] \\ B = \frac{\alpha X_m}{C_p}\left[\frac{(r\Omega)^2}{1+(r\Omega)^2}\right] \\ c(\theta) = \left[A\sin(\phi_{\text{sc}}) - B\cos(\phi_{\text{sc}})\right]\ e^{\frac{\phi_{\text{sc}}-\theta}{r\Omega}} \end{cases} \tag{10}$$

where r is the normalized resistance ($r = R\omega_0 C_p$). From the expression of the PEH voltage, the expression of ε_D and ε_K are obtained by calculating the first Fourier series coefficients of the PEH voltage (see Appendix). Unfortunately, no analytical solution exists for the expression of the optimal ϕ_0. As a result, it becomes necessary to numerically determine ϕ_0 and, consequently, the optimal short circuit duration $\Delta\phi_{\text{RSC}-opt}$ and normalized resistance $r_{\text{RSC}-opt}$. A workaround is proposed in the following section to address this issue.

Fig. 5 shows the performances obtained from the analytical model of the RSC interface compared with the classical RC interface and the resistive only R interface [10], [21]. For R, RC, and RSC, we superimpose the normalized power P_{norm} and their respective optimal parameters: $r_{\text{R}-opt}$ for R, $r_{\text{RSC}-opt}$, $\Delta\phi_{\text{RSC}-opt}$ for RSC and $r_{\text{RC}-opt}$, $c_{\text{RC}-opt}$ for RC with c the normalized capacitance $c = C/(C+C_p)$. The PEH, whose parameters are the same as those used in Section II, exhibits a high figure of merit ($k_m^2 Q = 15$) [30]. Fig. 5 also gives the simulated results of the RSC interface, very close to the analytical ones, obtained from a transient simulation using MATLAB/Simulink. It shows that the RC and RSC interfaces share the same performances in terms of bandwidth and maximum extracted power (with a common notation $P_{\text{RC/RSC}}$).

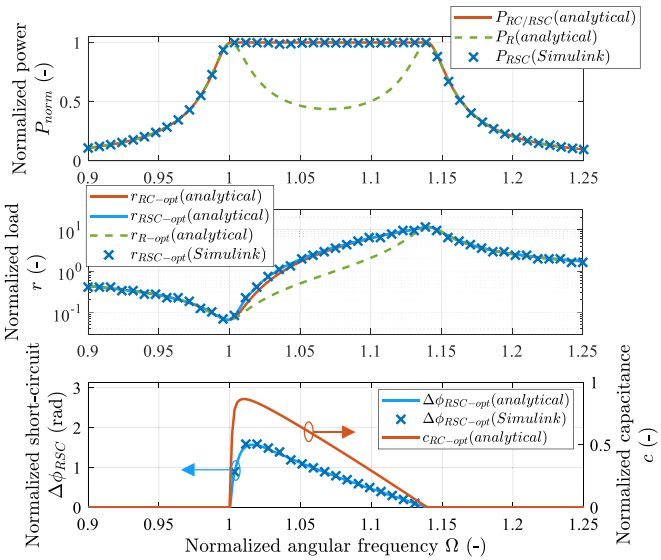

Fig. 5. Normalized extracted power $\boldsymbol{P}_{\text{norm}}$ for the RC, (analytical), R (analytical), and RSC (analytical and Simulink) interfaces and their optimal parameters for $\boldsymbol{k_m^2} = 0.3$, $\boldsymbol{Q} = 50$, $\boldsymbol{f}_{SC} = 26.9$ Hz, $\boldsymbol{C_p} = 25$ nF.

B. Optimal Parameters Calculation

We can see in Fig. 5 that the analytical optimal load for the RC interface ($r_{\text{RC}-opt}$) is very close to the RSC optimal load ($r_{\text{RSC}-opt}$). As we cannot obtain a closed-form expression of $r_{\text{RSC}-opt}$, we fix $R_{\text{RSC}-opt}$ to $R_{\text{RC}-opt}$, as shown in (11). Contrary to the $R_{\text{RSC}-opt}$ load, the expression of $R_{\text{RC}-opt}$ can easily be obtained as it is the resistance value that satisfies the equality between the real part of Z_{piezo} and the real part of the electrical interface Z_{elec}. One can mention that the power decrease introduced by this approximation increases with k_m^2, but it remains relatively small. As a matter of example, it remains less than 4% with $k_m^2 Q = 15$ only for a very limited range of the harvesting bandwidth

$$R_{\text{RSC}-opt} \approx R_{\text{RC}-opt} = 1/\text{Re}\left(1/Z_{piezo}\right). \tag{11}$$

As for the resistance, there is no closed-form solution for the optimal SC duration $\Delta\phi_{\text{RSC}-opt}$. On the basis of simulations, we can conjecture that there is only one optimal short circuit $\Delta\phi_{\text{RSC}-opt}$ per normalized impedance value $\widetilde{Z_{piezo}}$ on the useful frequency range $[\Omega_{\text{SC}} = 1,\ \Omega_{\text{OC}} = \sqrt{1+k_m^2}]$. This means that at any frequency, a calculation of the impedance $\widetilde{Z_{piezo}}$ can lead to obtaining $\Delta\phi_{\text{RSC}-opt}$ and, thus, reaching the maximum extracted power $P_{\text{norm}-\max}$ (knowing $R_{\text{RSC}-opt}$).

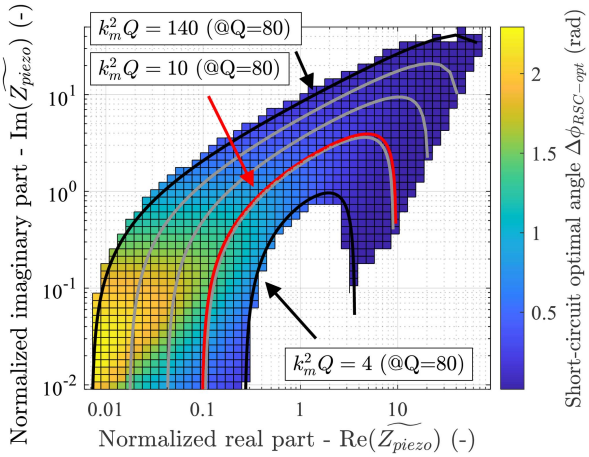

Fig. 6. In total, 50 × 50 map of SC angle versus normalized impedance $\boldsymbol{\widetilde{Z_{piezo}}}$. Lines for specific values of $\boldsymbol{k_m^2Q}$ are drawn on top of the map. Background color is equivalent to $\boldsymbol{\Delta\phi_{\mathrm{RSC}-opt} = 0}$ rad. Characteristics of our harvester, presented in Section V, are shown in red.

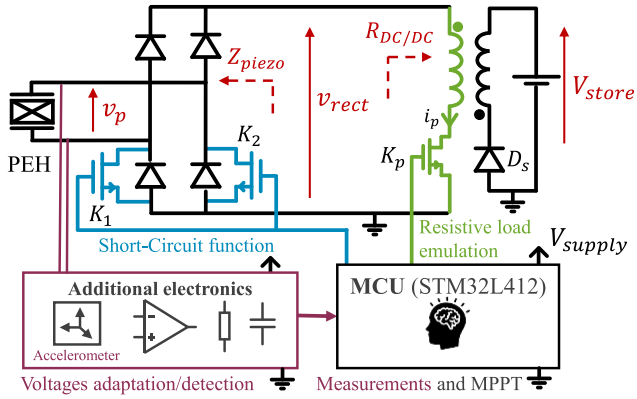

Fig. 7. Global architecture of the proposed power management circuit.

We can express this optimal solution as a function of Re($\widetilde{Z_{piezo}}$) and Im($\widetilde{Z_{piezo}}$). This leads to Fig. 6, which is a harvester-independent map containing the optimal SC angles $\Delta\phi_{\mathrm{RSC}-opt}$ corresponding to the normalized impedance $\widetilde{Z_{piezo}}$. The map shown in Fig. 6 is limited to values of $\widetilde{Z_{piezo}}$ corresponding to PEHs whose characteristic values k_m^2 and Q vary such that the product k_m^2Q is in the range 4 to 140, covering an extensive spectrum of existing PEHs. This encompasses the range of the most coupled PEHs found in the current SoA [16]. Here, we also presume that there is no practical benefit in implementing complex impedance matching for a PEH with a k_m^2Q figure of merit less than four.

In operation, for a specific harvester, the system only needs to know the value of the intrinsic capacitance C_p of the PEH (which is not supposed to vary during the PEH's lifetime), the current pulsation frequency ω and the harvester's impedance Z_{piezo} (obtained from the TLCM) to deduce the right optimal parameters of the RSC electrical interface. This mapping method is a crucial point in the operation of the proposed system. Indeed, this map, which is known by the algorithm before the system's start-up, is not restrictive to a given PEH (no need for k_m^2 or Q), and only its intrinsic capacitance C_p must be known beforehand.

This approach, based on measuring the impedance of the piezoelectric generator around an operating point and emulating the optimal load impedance, is robust to PEH aging and certain nonlinearities. The only assumption is the linearity of the given harvester around an operating point. Section IV describes how the proposed algorithm and electrical interface are implemented in a concrete manner, i.e., with an MCU-based power management circuit. Section V will later provide the experimental validation.

IV. Implementation

A. Global Architecture

To implement the proposed architecture, i.e., the aforementioned MPPT algorithm (TLCM method) along with its electrical interface (RSC), we used a MCU surrounded by discrete electronics. The choice of using off-the-shelf components (COTS) can be viewed as either 1) a more flexible and less complex solution than a specific ASIC or 2) as relevant in specific applications that have not yet reached a mass market. As depicted in Fig. 7 additional electronics, including a low-power accelerometer used to measure the phase difference between the PEH voltage and the input acceleration, two comparators as well as an external low-power clock, surround a STM32L412 MCU (ST Microelectronics). The external clock is feeding independent peripherals of the MCU for low-power purposes. Concerning the power path, the PEH is connected to a full bridge rectifier (FBR) followed by a Flyback converter controlled by the MCU in discontinuous current mode (DCM). The Flyback does not only emulate the chosen resistive load (R becomes $R_{\mathrm{dc-dc}}$) at the primary side (v_{rect}) but it also transfers and converts the electrical power to the storage element (V_{store}). Here, the emulation of a resistive load along with a rectifier does not change the optimal values of the RSC interface (without rectifier) nor does it change the calculation of Z_{piezo} with the TLCM. The SC function is performed by the MCU, which controls the two NMOS K_1 and K_2 at the bottom of the FBR. A load emulation waveform with SC is shown Fig. 8. The subsequent sections provide a more in-depth exploration of these functions.

B. Impedance Emulation

1) Resistive Load Emulation: The real part of the optimal impedance Z_{opt} is emulated thanks to a Flyback converter operating in DCM mode, as given in (12), which gives the resulting resistive load $R_{\mathrm{dc-dc}}$ emulated by the Flyback [32], [33]

$$R_{dc-dc} = \frac{2L}{f_{dc-dc}t_{\mathrm{on}}^2}. \tag{12}$$

With L the inductance value of the primary side (10 mH, RN216-1-02-10M), $f_{\mathrm{dc-dc}}$ the PWM switching frequency of the Flyback (K_p control) and t_{on} the on-time of the PWM. The Flyback topology was selected for its simplicity in switch operation, enabling the use of low voltage levels for the control signals. Moreover, it produces a positive output voltage, and its emulated resistance remains independent of both the input and output voltages [32], [33]. In our work, the value of $R_{\mathrm{dc-dc}}$ is

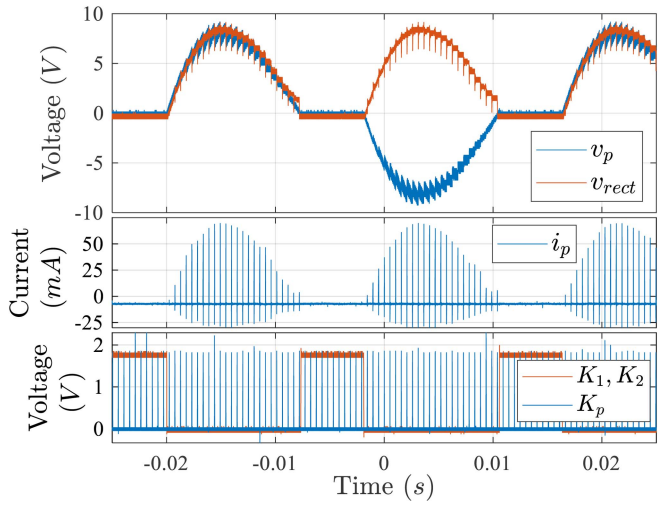

Fig. 8. Measured voltage and current waveforms of the RSC interface at $f_{\text{input}} = 27.5$ Hz with $R_{\text{dc-dc}} = 100$ kΩ ($t_{\text{on}} = 10$ μs, $f_{\text{dc-dc}} = 2$ kHz) and $\Delta\phi_{\text{RSC}} = 1$ rad.

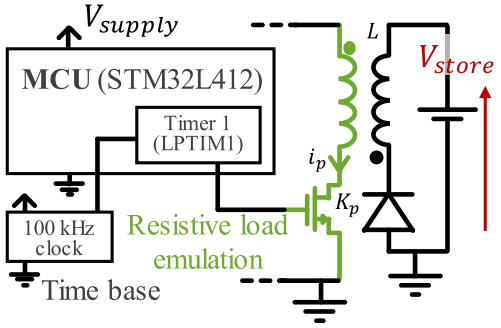

Fig. 9. Resistive load emulation part of the proposed implementation.

adjusted from varying the switching frequency $f_{\text{dc-dc}}$, while the on-time is maintained constant. Compared to its varying$-t_{\text{on}}$ counterpart, variable frequency PWM enables a lower input clock speed for the same resistance resolution [34], thereby reducing power consumption. Fixing $t_{\text{on}} = 10\,\mu$s, the system emulates resistive load values within the 10 kΩ to 1 MΩ range for $f_{\text{dc-dc}}$ in the 200 Hz to 20 kHz range. As shown in Fig. 9, the PWM is generated by the MCU from an independent low-power timer (Timer 1), fed by the external low-power 100 kHz clock (OM-0100-C8) to reduce the overall power consumption.

As detailed in Section II, we need to emulate the measurement loads R_1 and R_2. As a design tradeoff (between energy harvesting and precision of measurement) and for ease of implementation, we will set these loads to the boundaries of the emulated resistor range ($R_1 = 10$ kΩ and $R_2 = 1$ MΩ) as a way to encompass the PEH impedance for the entire operating frequency range.

2) Short-Circuit Function: As described in Section III, the imaginary part of the optimal impedance Z_{opt} is emulated thanks to a controlled duration SC starting at the zero-crossing voltage instant. This SC function (see Fig. 10), performed by turning K_1 and K_2 on is also controlled thanks to a low-power timer (Timer 2) of the MCU fed by the 100 kHz clock mentioned previously,

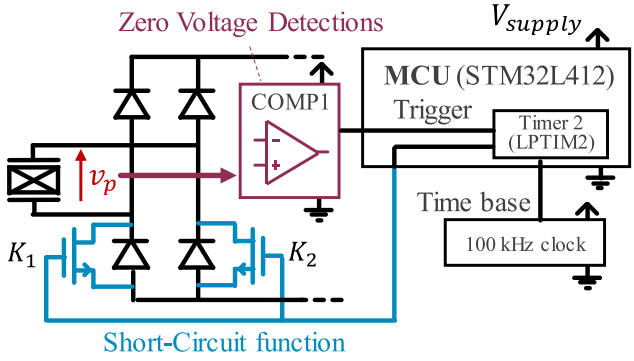

Fig. 10. Implementation of the SC function.

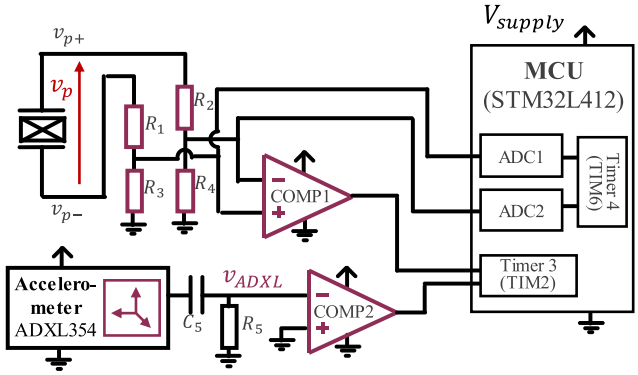

Fig. 11. Timing measurements for the proposed MCU-based implementation of the TLCM.

giving a 10 μs time resolution for the SC duration. A low-power comparator (TS881) is used to detect the zero crossing of the PEH voltage and to launch the SC function.

The proposed RSC interface significantly improves the compactness of the power management circuit stage, eliminating the need for a bank of discrete capacitors to compensate for the reactive part of Z_{piezo}. Furthermore, the hardware choices allow the emulation of a complex impedance in a very low-power manner, i.e., below 22 μW under 1.8 V. The measurements results are given in Section V.

C. Measurements Needed for the TLCM

1) Phase Measurement: To estimate the optimal impedance Z_{opt} to emulate, the proposed MPPT algorithm must evaluate the phase difference between the input acceleration and the PEH voltage. As shown in Fig. 11, the phase difference is obtained by measuring the duration between two zero crossing detectors: one from of the input acceleration (COMP2) and the other from the PEH voltage (COMP1). To that end, a low-power analog accelerometer (ADXL354) feeds COMP2 only during the measurement phase (consuming ∼150 μA when activated). The duration between COMP1 and COMP2's rising edges is measured thanks to a timer (Timer 3). Its time base is the internal clock of the MCU reduced to its minimum value (200 kHz) for a low-power purpose, giving a time resolution of 5 μs.

2) Voltage Measurement: To determine the optimal impedance Z_{opt}, the proposed MPPT algorithm must also evaluate

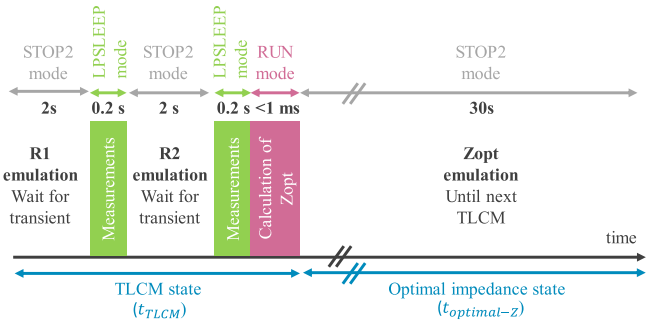

Fig. 12. Temporal description of the proposed MPPT algorithm with its associated low-power modes (not to scale).

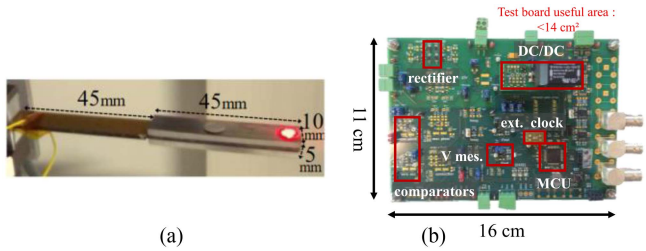

Fig. 13. (a) PMN-PT based PEH with (b) associated test board.

TABLE I
CHARACTERISTICS OF THE PEH

Piezoelectric capacitance (C_p)	41.9 nF
Effective mass (M)	15.2 g
Short-circuit resonant frequency (f_{sc})	26.9 Hz
Spring constant (K)	434.2 N/m
Damping coefficient (D)	33.8 mN/m/s
Electromechanical coupling coeff. (k_m^2)	13 %

the PEH voltage. As seen in Fig. 11, the MCU measures the PEH voltage v_p (i.e., before the full bridge rectifier) by means of a differential voltage measurement ($v_p = v_{p+} - v_{p-}$). The reason why the rectified voltage was not used is that a small portion of the energy remains at the primary side of the Flyback after its opening, leading to incorrect measurements of v_{rect} [35]. The voltage measurements are triggered by a MCU timer (Timer 4) at 1 kHz and two voltage dividers reduce v_{p+} and v_{p-} to appropriate voltage levels (i.e., below 1.8 V). One should mention that the system is measuring v_p and not the load voltage v_{rect}, thus, we need to subtract the diode voltage drop to have an image of v_{rect} (the diode voltage drop cannot be neglected here).

3) Optimal Parameters Calculation: The calculation of the optimal parameters of the RSC interface (i.e., $R_{\text{RSC}-opt}$ and $\Delta\phi_{\text{RSC}-opt}$) is performed by the MCU right after the measurement phase. Having an estimation of the PEH impedance Z_{piezo} (from the TLCM voltage and phase measurement), the current vibration frequency (measured during the phase measurement step) and the PEH capacitance C_p (prestored value), the MCU calculates the optimal parameters thanks to the harvester-independent map detailed before (see Section III). The PEH capacitance is the only harvester dependent value that must be known and stored by the MCU before startup. In practical terms, those parameters are prestored in a 2d array as unsigned 8 bits integers (50×50 size). The values of real and imaginary normalized impedance $\widetilde{Z_{piezo}}$ are stored as floating-point numbers (2×50 size). This leads to an overall small size array of 5.7 kB, i.e., $\sim$15% of the total RAM of the STM32L412.

D. MCU States

To reach a very low power consumption compatible with the PEH output powers, we performed low-level programming to optimize the power modes of the MCU. Fig. 12 describes the temporality of the power modes and their link to the system's cadence and states. The duration given for each power mode is specific to the harvester that will be introduced in the following section and should be adapted for other harvesters (especially t_{TLCM}). As seen in Fig. 12, the MCU alternates between two different states: the TLCM state (t_{TLCM}), during which the optimal impedance is calculated and the optimal impedance state ($t_{\text{optimal}-Z}$), during which the harvested energy is maximized.

The TLCM duty-cycle dc_{TLCM} [see (13)] is fixed to 13% in this article

$$\text{dc}_{\text{TLCM}} = t_{\text{TLCM}} \,/\, (t_{\text{optimal}-Z} + t_{\text{TLCM}})\,. \tag{13}$$

When the TLCM state is not executed, the MCU remains in very low power mode, i.e., the lowest power mode of the MCU while retaining RAM ("STOP2" mode of the STM32: $\sim$0.7 μA @ 1.8 V). During this state, the MCU is nonetheless capable of generating the PWM signals to emulate the optimal impedance Z_{opt} with the RSC interface ("Optimal impedance state" in Fig. 12). After a specified refresh time (see Fig. 12), an internal low-power oscillator wakes the MCU up, switching to the TLCM state. In this state, the MCU operates mainly in "STOP2" mode. It then controls the successive emulation of the two different measurement resistive loads (R_1 and R_2) required to calculate the PEH impedance. As the transients of the system are governed by the mechanical quality factor of the system, the MCU must wait several mechanical periods before reaching a mechanical steady state (2 s in our case). After two transients for resistors R_1 and R_2 (see Fig. 12), the MCU makes the phase and voltage measurements in low-power mode ("LPSLEEP" mode of the STM32: $\sim$18.5 μA @ 1.8 V). Right after, computational tasks to calculate Z_{PEH} are performed with the lowest dynamic power consumption of the MCU ("RUN mode": 79 μA/MHz @ 1.8 V) for a period lower than 1 ms.

V. EXPERIMENTAL RESULTS

A. Experimental Setup and Testing Board

The performance of the proposed MPPT algorithm was evaluated with a highly coupled PEH [see Fig. 13(a)] having a coupling coefficient $k_m^2 = 13\%$. Following the method described in [12], its parameters (see Table I) are determined from its impedance measured with an impedance analyzer (Keysight E4990A).

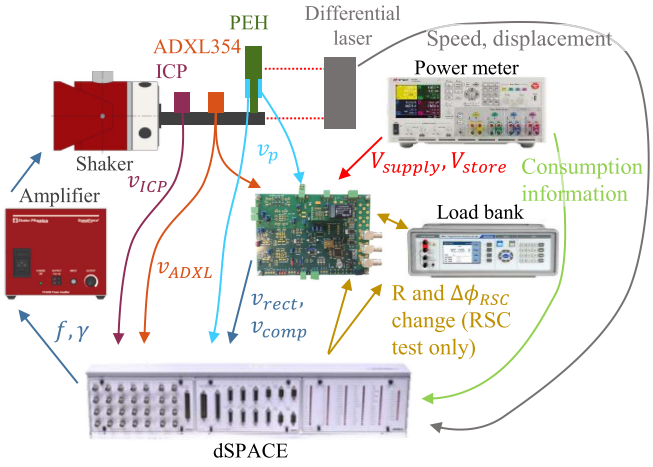

Fig. 14. Representation of the experimental setup used for vibration testing: RSC interface testing (test board with load bank) and autonomous mode (test board only). Other laboratory equipment is for monitoring purposes only.

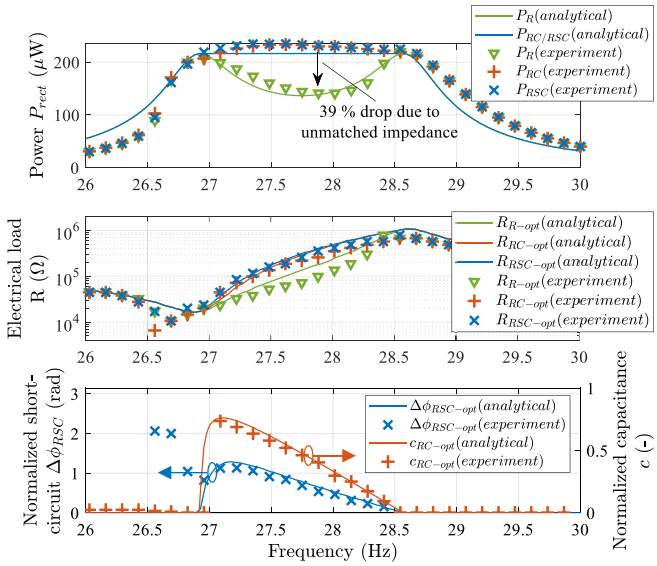

Fig. 15. Analytical and experimental optimal extracted power ($\boldsymbol{P_{rect}}$) for the R, RC, and proposed RSC electrical interface.

The test board used to test the MPPT [see Fig. 13(b)] embeds the microcontroller and all the associated hardware (see Section IV). The total size of the circuit board is 176 cm^2 but the useful area on the board is relatively small (less than 14 cm^2) as it contains other unimplemented features for testing purposes that could be removed in a future compact version of the circuit.

A test bench was built in association with a dSPACE control platform and MATLAB/Simulink (see Fig. 14). This test bench was used to 1) experimentally verify the operation of the RSC electrical interface (see Section V-B) and to 2) monitor the operation of the autonomous MPPT and RSC interface inside the test board (see Sections V-C and V-D). The dSPACE platform is linked to the STM32L4 MCU via a serial port. An electromagnetic shaker (K2075E-HT) generates the input acceleration. It is driven in closed loop by the dSPACE platform to regulate the input acceleration, which is measured by an accelerometer (ICP 352C68). The dSPACE platform is controlled by a dedicated MATLAB script that defines the acceleration level and frequency. To check the proper operation of the MPPT algorithm, the dSPACE board also acquire all the useful signals (v_p, v_{rect}, v_{ADXL}, v_{ICP}, comparators outputs v_{comp}) during the experiments.

The power extracted from the PEH P_{rect} is measured thanks to the dSPACE platform (only for Section V-B), we assume that the power lost to the diode bridge is negligible. A N6705B dc power analyzer was used to measure the power consumption of the circuit P_{supply} as well as the harvested power P_{store} and, hence, the efficiency of the Flyback converter. The experiments have been done for an acceleration of 0.5 m/s^2 peak, over 31 excitation frequencies ranging from 26 Hz to 30 Hz.

B. Extracted Power With the RSC Electrical Interface

The RSC interface was first validated experimentally without using the MPPT algorithm by testing different parameters ($\Delta\phi_{\text{RSC}}$, R) with discrete resistive loads. The SC is emulated by the MCU while the load is emulated by a M642 resistance box. A post processing was performed to keep the optimal parameters maximizing the extracted power P_{rect}. For comparison, the same experiment was accomplished for the R and RC interfaces. In the case of the R interface, the optimal resistance values correspond to the absolute value of the PEH output impedance $R = |Z_{piezo}|$. These results are plotted on Fig. 15. The experimental optimal parameters and power results are in quite good agreement with the ones predicted by the linear model. The difference (mainly on the power, and before the first resonant frequency for the SC angle) undoubtedly comes from nonlinear behaviors in the PEH (softening behavior probably due to the use of PMN-PT material [12], [36]). The experimental power response of the RC and RSC interfaces show their ability to compensate for the inductive part of the PEH between $f_{SC} = 26.9$ Hz and $f_{OC} = 28.6$ Hz.

C. Temporal Measurements and Power Consumption of the Proposed MPPT

This section presents an illustrative case of the temporal behavior exhibited by the proposed MPPT in response to a change in frequency within the useful PEH bandwidth. The system is fully self-powered and the dSPACE board is only used to record useful signals and control the acceleration. As depicted in the measurements of Fig. 16, we manually adjusted the input frequency at time 47 s, reducing it from $f_A = 28.75$ Hz to $f_B = 27.75$ Hz. Immediately following this frequency change, the harvested power (P_{store}) drops by ~74%, indicating that the optimal parameters established for the RSC interface at f_A were no longer optimal for f_B. Indeed, referring to Fig. 15, the previously identified optimal parameters at f_A were approximately $R_{\text{dc-dc}} = R_{\text{RSC}-opt} = 454$ kΩ with no SC ($\Delta\phi_{\text{RSC}} = \Delta\phi_{\text{RSC}-opt} = 0$) whereas the new optimal parameters for f_B are $R_{\text{dc-dc}} = R_{\text{RSC}-opt} = 526$ kΩ with $\Delta\phi_{\text{RSC}} = \Delta\phi_{\text{RSC}-opt} = 0.9$ rad. Subsequently, after the next refresh period around time $t = 52$ s, the system transitions into the TLCM state, triggering a recalculation of the optimal impedance as

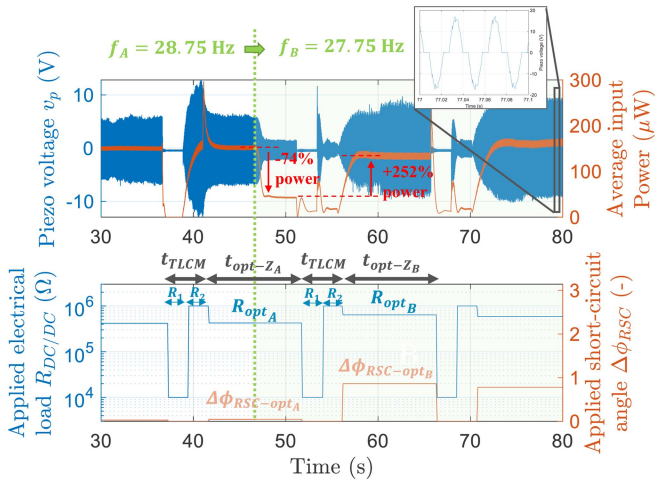

Fig. 16. Example of measured waveforms for the proposed architecture (MPPT + RSC interface). PEH voltage $\boldsymbol{v_p}$ and harvested power on $\boldsymbol{V}_{\text{store}}$ (top plot), as well as applied parameters $\boldsymbol{R}_{\text{dc-dc}}$ and $\boldsymbol{\Delta}\phi_{\text{RSC}}$ (bottom plot), as a function of time, if the input frequency is reduced from 28.75 Hz to 27.75 Hz ($\text{dc}_{\text{TLCM}} = 30\%$ for greater figure clarity).

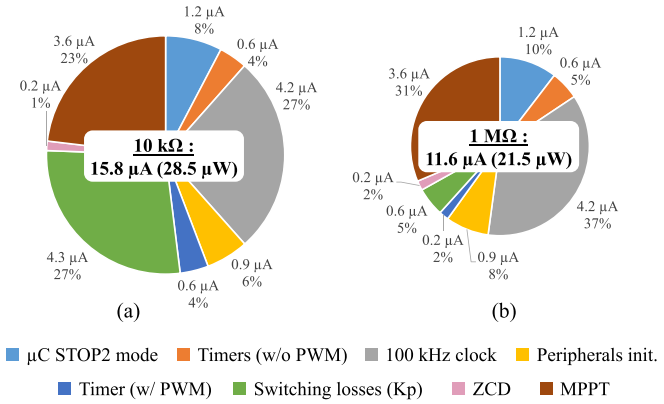

Fig. 17. Overall power consumption $\boldsymbol{P}_{\text{supply}}$ of the proposed circuit when the Flyback converter emulates (a) a 10 kΩ load and (b) a 1 MΩ load ($\text{dc}_{\text{TLCM}} = 13\%$).

well as the new parameters, leading to a subsequent increase in the harvested power, close to the maximum power for f_B, i.e., around 160 μW.

Fig. 17 shows the power consumption breakdown of the whole system for two different resistances $R_{\text{dc-dc}}$ emulated by the Flyback. During the optimal impedance state (STOP2 mode), the system consumes around 22 μW ($R_{\text{dc-dc}} = 10$ kΩ) and 15 μW ($R_{\text{dc-dc}} = 1$ MΩ). This consumption indeed depends on the PWM frequency of the Flyback converter. One should mention that the SC function has a negligible impact on the power consumption. The power consumption attributed to the MPPT function (i.e., the TLCM) represents 23% to 31% of the total power consumption P_{supply} of our system when activated with $\text{dc}_{\text{TLCM}} = 13\%$.

D. Harvested Power With the Proposed MPPT

To quantify the harvested power and bandwidth performances of the proposed MPPT autonomously, the same experiment

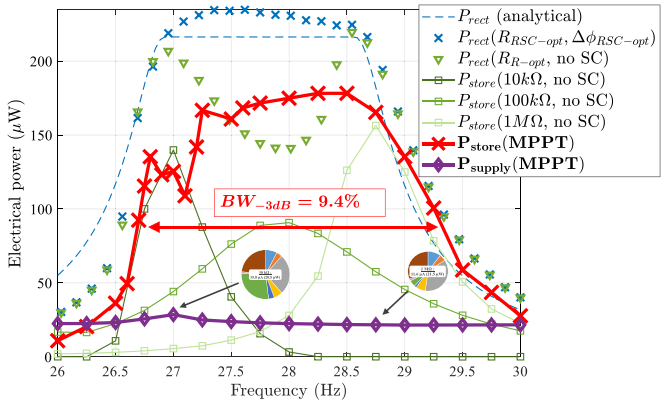

Fig. 18. Electrical power as a function of the input frequency. Theoretical and extracted power with discrete R (blue), experimental harvested power with a fixed and optimal $\boldsymbol{R}_{\text{dc-dc}}$ (green curves) and experimental harvested power with the proposed MPPT and RSC interface (red) as well as the power consumption of the system (purple). Pie charts are the ones of Fig. 17 ($\text{dc}_{\text{TLCM}} = 13\%$).

was reproduced within the whole useful frequency band of the PEH. In this case, we change the input frequency from 26 Hz to 30 Hz by steps of 0.25 Hz. The average harvested power (P_{store}) is measured for the combined TLCM and optimal impedance states. Fig. 18 shows the harvested power and power consumption (P_{supply}) of the whole system. The power consumed by the system is always lower than 28.5 μW. The harvested power peaks at 178 μW giving a minimal usable power of about 150 μW. For comparison, the measured rectified extracted power (P_{rect}) obtained with the optimal parameters (discrete $R_{\text{RSC}-opt}$ and $\Delta\phi_{\text{RSC}-opt}$) is plotted, underlying the conversion efficiency of the Flyback converter ($\eta_{\text{dc-dc}} = P_{\text{store}}/P_{rect}$). This efficiency goes from ~65% to ~80%. The obtained bandwidth of 9.4%, while depending on the harvester properties (k_m^2 and Q), was not decreased by the combination of our circuit with the MCU-based MPPT algorithm (compared to the optimal extracted power). Only the maximum power was reduced due to the converter's efficiency and power consumption of the system. Fig. 18 also shows a comparison of our solution with the simple R interface (using the Flyback dc–dc converter to emulate $R_{\text{dc-dc}}$) with three fixed resistors (10 kΩ, 100 kΩ, and 1 MΩ). It illustrates that the proposed approach leads to an extended bandwidth (35% more) and a higher power. For example, using a fixed 100 kΩ emulated resistor, the bandwidth is around 7.1% with only 91 μW maximum harvested power. Finally, we observe that while the obtained power is approximately flat between the two resonant frequencies, suboptimal parameters are found near the SC frequency (27 Hz), leading to a slight power drop. This problem is due to the lower resolution of the voltage measurement when the piezoelectric impedance is low (it is minimal at $f = f_{SC}$).

VI. Discussion

Table II shows a comparison between several articles of the MPPT algorithms for strongly coupled PEH state of the art. We emphasize on several important parameters about the MPPT algorithm such as its speed (in mechanical cycles normalized

TABLE II
COMPARISON WITH STATE OF THE ART

Ref.	ISSCC'18 [24]	JIMSS'22 [28]	ISSCC'20 [25]	TCAS'20 [26]	ISCAS'20 [29]	TPEL'23 [44]	ECM'24 [45]	**This work**
Technology	Integrated (0.35 μm)	Simulation and dSPACE experiment	Integrated (0.35 μm)	MCU	Integrated (0.25 μm)	MCU	MCU	MCU
Transducer type	PEH	PEH	PEH	PEH	PEH	EEH	PEH	PEH
Resonant Frequency f_{res} [Hz]	90	94	56	160	291	89	37	27
Mechanical quality factor Q	-	20	25	96 *	-	104 **	160	78
Harvesting strategy (Nb of tuning parameters)	**FTSECE (2)**	**SCSECE (2)**	PS-SECE (1)	**PWM rectifier (2)**	**PS-SSHI (2)**	**PWM rectifier (2)**	**FT-OSECE (2)**	**RSC (2)**
MPPT strategy	LUT	DOCT	P&O	P&O	Impedance measurement (no ambient acc.)	P&O	P&O	TLCM
Harvester's dependent knowledge	optimal couple of the PS-SECE strategy	optimal couple of the SCSECE strategy	**none**	**none**	**none**	EEH coil resistance and inductance	**none**	PEH capacitance because of the RSC strategy
Number of mechanical cycles to reach MPP	**None (fixed)**	5Q cycles (fixed)	32Q cycles * (variable)	26Q cycles * (variable)	**1Q cycle * (fixed)**	23Q cycles * (variable)	48Q cycles (variable)	**2Q cycles (fixed)**
Time to reach MPP [s] @f_{res}	**none**	1	14 *	16 *	**-**	28 *	220	**4.4**
Inductance value [μH]	>2000 *	-	**220**	100000	1000	1030	1000	10000
Robust to the generator's parameters variation	no	yes / no	**yes**	**yes**	**yes**	**yes**	**yes**	**yes**
Maximum voltage rating [V]	5 *	-	20	-	-	-	**100**	**60**
Additional mechanical sensors	**none**	**none**	**none**	accelerometer	**none**	**none**	piezoelectric patches	accelerometer
Power consumption [μW]	**0.38**	-	**<1**	-	-	1790	63.71	21.5 - 28.5
Max extracted power [μW]	73.4 @1g	-	210 @0.1g peak	1800 @0.6g peak	14.14 @0.1g	10110 @ 0.3g	712.5 @0.05g peak	235 @0.05g peak

*Estimated from paper,
**calculated from paper

by the mechanical quality factor Q), its robustness and the predetermined parameters needed for it to perform properly. The speed comparison of the different MPPT algorithms assumes that if a measurement needs to be made, the time needed for it is negligible compared to the mechanical transient time. In this table, we do not compare our work with FOCV-based [37], [38] and P&O-based algorithms regulating the conduction angle [39], [40] as their corresponding electrical interfaces are not efficient to emulate the optimal impedance Z_{opt} in the case oh highly-coupled PEH (the optimal voltage for the SEH and the pSSHI electrical interfaces is not always half of the open-circuit voltage: $V_{OC}/2$ [41]).

First, our MPPT algorithm is fast compared to the state of the art (up to 13 times faster than another 2 parameters P&O MPPT [26]). Its convergence time is also fixed and does not depend on the starting parameter as in P&O algorithms. Because our MPPT implementation is based on an impedance measurement, it is robust to any mechanical variation in the PEH (due to temperature variation or aging) contrary to LUT implementation [24]. Moreover, the TLCM works even when ambient vibration is present in contrast to the strategy proposed in [29] where measurements must be performed at no-vibration, limiting its practical application. TLCM and DOCT algorithms quickly converge even when the starting point is far from the optimal one. The proposed TLCM is, however, at least two times faster than DOCT and requires less knowledge on the PEH. The only drawback with respect to LUT only is that the PEH does not operate at its MPP when doing the measurements. Eventually, mutualizing the MCU to implement the proposed MPPT and some functions of the wireless sensor node would be an interesting optimization from a cost and area standpoint compared to the classical ASIC plus MCU implementation.

Finally, the bandwidth obtained with the proposed electrical interface is as good as with the RC electrical interface. Compared to the latter, the proposed interface gives an improved power density since it does not need several discrete capacitors and their associated switches. In contrast to SEH, pSSHI, sSSHI, or SECE electrical interfaces [37], [42], [43] our RSC (RC like) interface exhibits a larger maximum bandwidth or extractable power with highly coupled PEH as described in review papers [10], [23].

At last, the power consumption of our MCU implementation is lower than other MCU-based MPPT algorithms used with frequency tuning electrical interfaces [26], [44], [45]. Compared to ASIC based solutions [24], [25], [29], our work consumes however more power. Nevertheless, other optimizations could reduce the TLCM consumption. For example, it would be relevant to start the TLCM only when there if a frequency change, thus reducing the power consumption when the input frequency changes slowly (drastically reducing dc_{TLCM}).

VII. CONCLUSION

In this article, a complete piezoelectric energy harvesting system is shown, which is made of a new electrical interface, the RSC, associated with a fast and robust maximum power point algorithm: the TLCM. The RSC shows the same harvesting bandwidth (9.4%) as the RC interface without requiring a full

capacitance bank. The peak harvested power is of 178 μW (while the peak extracted power is 235 μW) with a maximum of 28.5 µW of power consumption for the whole circuit. The efficiency of the Flyback converter is between 65% to 80%. The TLCM finds the optimal parameters needed for the MPP almost in the closest time compared to other robust algorithms with two parameters electrical interfaces (up to 13 times faster).

In the future, automatic capacitance measurement could be implemented as to be completely independent of the associated PEH. The TLCM timing should also be adapted to other resonant frequencies and mechanical quality factors. Finally, the TLCM has been characterized here only under sinusoidal oscillations. Future work will then focus on the study of TLCM in the case of non-sinusoidal excitation.

APPENDIX

The expressions of ε_D and ε_K of the RSC electrical interface are given below. They are obtained solving (9) to find the first Fourier series coefficient

$$\begin{aligned}
\varepsilon_D = {} & \left(\Omega r\left(2\Phi_0 - 2\Phi_{SC} - \sin\left(2\Phi_0\right) + \sin\left(2\Phi_{SC}\right)\right.\right. \\
& - 4\Omega r + 2\Omega^3 r^3 \cos(\Phi_0)^2 + 2\Omega^3 r^3 \cos(\Phi_{SC})^2 \\
& - \Omega^2 r^2 \sin\left(2\Phi_0\right) + \Omega^2 r^2 \sin\left(2.\Phi_{SC}\right) + 2\Omega^2 r^2 \Phi_0 \\
& - 2\Omega^2 r^2 \Phi_{SC} + 2\Omega r \cos(\Phi_0)^2 + 2\Omega r \cos(\Phi_{SC})^2 \\
& - 4\Omega^3 r^3 \exp\left(-\frac{\Phi_0 - \Phi_{SC}}{\Omega r}\right) \cos\left(\Phi_0\right) \cos\left(\Phi_{SC}\right) \\
& + 4\Omega^2 r^2 \exp\left(-\frac{\Phi_0 - \Phi_{SC}}{\Omega r}\right) \cos\left(\Phi_0\right) \sin\left(\Phi_{SC}\right) \\
& - 4\Omega^2 r^2 \exp\left(-\frac{\Phi_0 - \Phi_{SC}}{\Omega r}\right) \cos\left(\Phi_{SC}\right) \sin\left(\Phi_0\right) \\
& \left.\left. + 4\Omega r \exp\left(-\frac{\left(\Phi_0 - \Phi_{SC}\right)}{\Omega r}\right) \sin\left(\Phi_0\right) \sin\left(\Phi_{SC}\right)\right)\right) \\
& \Big/\left(2\pi\left(\Omega^2 r^2 + 1\right)^2\right) \\
\varepsilon_K = {} & \left(\Omega r\left(2\cos(\Phi_0)^2 - 2\cos(\Phi_{SC})^2 - 4\Omega^2 r^2\right.\right. \\
& + 2\Omega^2 r^2 \cos(\Phi_0)^2 - 2\Omega^2 r^2 \cos(\Phi_{SC})^2 + \Omega^3 r^3 \sin\left(2\Phi_0\right) \\
& + \Omega^3 r^3 \sin\left(2\Phi_{SC}\right) + 2\Omega^3 r^3 \Phi_0 - 2\Omega^3 r^3 \Phi_{SC} \\
& + \Omega r \sin\left(2\Phi_0\right) + \Omega r \sin\left(2\Phi_{SC}\right) + 2\Omega r \Phi_0 - 2\Omega r \Phi_{SC} \\
& + 4\Omega^2 r^2 \exp\left(\frac{\Phi_{SC} - \Phi_0}{\Omega r}\right) \cos\left(\Phi_0\right) \cos\left(\Phi_{SC}\right) \\
& - 4\Omega^3 r^3 \exp\left(\frac{\Phi_{SC} - \Phi_0}{\Omega r}\right) \cos\left(\Phi_{SC}\right) \sin\left(\Phi_0\right) \\
& + 4\Omega^2 r^2 \exp\left(\frac{\Phi_{SC} - \Phi_0}{\Omega r}\right) \sin\left(\Phi_0\right) \sin\left(\Phi_{SC}\right) \\
& \left.\left. - 4\Omega r \exp\left(\frac{\Phi_{SC} - \Phi_0}{\Omega r}\right) \cos\left(\Phi_0\right) \sin\left(\Phi_{SC}\right)\right)\right) \\
& \Big/\left(2\pi\left(\Omega^2 r^2 + 1\right)^2\right).
\end{aligned}$$

REFERENCES

[1] J. Siang, M. h. Lim, and M. Salman Leong, "Review of vibration-based energy harvesting technology: Mechanism and architectural approach," *Int. J. Energy Res.*, vol. 42, no. 5, pp. 1866–1893, 2018, doi: 10.1002/er.3986.

[2] P. Gasnier et al., "A 120°C 20G-compliant vibration energy harvester for aeronautic environments," *J. Phys., Conf. Ser.*, vol. 1407, no. 1, Nov. 2019, Art. no. 012118, doi: 10.1088/1742-6596/1407/1/012118.

[3] K. V. Selvan and M. S. Mohamed Ali, "Micro-scale energy harvesting devices: Review of methodological performances in the last decade," *Renewable Sustain. Energy Rev.*, vol. 54, pp. 1035–1047, Feb. 2016, doi: 10.1016/j.rser.2015.10.046.

[4] E. Arroyo, A. Badel, F. Formosa, Y. Wu, and J. Qiu, "Comparison of electromagnetic and piezoelectric vibration energy harvesters: Model and experiments," *Sensors Actuators A, Phys.*, vol. 183, pp. 148–156, Aug. 2012, doi: 10.1016/j.sna.2012.04.033.

[5] M. Safaei, H. A. Sodano, and S. R. Anton, "A review of energy harvesting using piezoelectric materials: State-of-the-art a decade later (2008–2018)," *Smart Mater. Struct.*, vol. 28, no. 11, Oct. 2019, Art. no. 113001, doi: 10.1088/1361-665X/ab36e4.

[6] S. M. Shahruz, "Design of mechanical band-pass filters for energy scavenging," *J. Sound Vib.*, vol. 292, no. 3–5, pp. 987–998, May 2006, doi: 10.1016/j.jsv.2005.08.018.

[7] Q. Demouron, A. Morel, D. Gibus, A. Benhemou, and A. Badel, "Performance enhancement of bistable piezoelectric energy harvesters using non-linear energy extraction circuit," in *Proc. 21st Int. Conf. Micro Nanotechnol. Power Gener. Energy Convers. Appl.*, Salt Lake City, UT, USA, 2022, pp. 58–61, doi: 10.1109/PowerMEMS56853.2022.10007580.

[8] C. Saint-Martin et al., "Optimized and robust orbit jump for nonlinear vibration energy harvesting," *Nonlinear Dyn.*, vol. 112, pp. 3081–3105, 2024, doi: 10.21203/rs.3.rs-2799325/v1.

[9] C. Eichhorn, F. Goldschmidtboeing, and P. Woias, "Bidirectional frequency tuning of a piezoelectric energy converter based on a cantilever beam," *J. Micromech. Microeng.*, vol. 19, no. 9, Sep. 2009, Art. no. 094006, doi: 10.1088/0960-1317/19/9/094006.

[10] A. Morel et al., "A comparative study of electrical interfaces for tunable piezoelectric vibration energy harvesting," *Smart Mater. Struct.*, vol. 31, no. 4, Apr. 2022, Art. no. 045016, doi: 10.1088/1361-665X/ac54e8.

[11] L. Tang, Y. Yang, and C. K. Soh, "Broadband vibration energy harvesting techniques," in *Advances in Energy Harvesting Methods*, N. Elvin and A. Erturk, Eds., New York, NY, USA: Springer, 2013, pp. 17–61, doi: 10.1007/978-1-4614-5705-3_2.

[12] D. Gibus et al., "Strongly coupled piezoelectric cantilevers for broadband vibration energy harvesting," *Appl. Energy*, vol. 277, Nov. 2020, Art. no. 115518, doi: 10.1016/j.apenergy.2020.115518.

[13] P.-H. Hsieh, C.-H. Chen, and H.-C. Chen, "Improving the scavenged power of nonlinear piezoelectric energy harvesting interface at Off-resonance by introducing switching delay," *IEEE Trans. Power Electron.*, vol. 30, no. 6, pp. 3142–3155, Jun. 2015, doi: 10.1109/TPEL.2014.2334611.

[14] B. Zhao, J. Liang, and K. Zhao, "Phase-variable control of parallel synchronized triple bias-flips interface circuit towards broadband piezoelectric energy harvesting," in *Proc. IEEE Int. Symp. Circuits Syst.*, Florence, Italy, 2018, pp. 1–5, doi: 10.1109/ISCAS.2018.8351800.

[15] C. Xie, G. Zhao, Y. Ma, M.-K. Law, and M. Zhang, "Fully integrated frequency-tuning switched-capacitor rectifier for piezoelectric energy harvesting," *IEEE J. Solid-State Circuits*, vol. 58, no. 8, pp. 2337–2348, Aug. 2023, doi: 10.1109/JSSC.2023.3261301.

[16] D. Gibus, A. Morel, P. Gasnier, A. Ameye, and A. Badel, "High performance piezoelectric vibration energy harvesting by electrical resonant frequency tuning," *Smart Mater. Struct.*, vol. 31, no. 12, Dec. 2022, Art. no. 125012, doi: 10.1088/1361-665X/ac9d74.

[17] A. Badel and E. Lefeuvre, "Wideband piezoelectric energy harvester tuned through its electronic interface circuit," *J. Phys., Conf. Ser.*, vol. 557, Nov. 2014, Art. no. 012115, doi: 10.1088/1742-6596/557/1/012115.

[18] A. Brenes et al., "Large-bandwidth piezoelectric energy harvesting with frequency-tuning synchronized electric charge extraction," *Sensors Actuators A, Phys.*, vol. 302, Feb. 2020, Art. no. 111759, doi: 10.1016/j.sna.2019.111759.

[19] A. Morel, P. Gasnier, Y. Wanderoild, G. Pillonnet, and A. Badel, "Short circuit synchronous electric charge extraction (SC-SECE) strategy for wideband vibration energy harvesting," in *Proc. IEEE Int. Symp. Circuits Syst.*, 2018, pp. 1–5, doi: 10.1109/ISCAS.2018.8351559.

[20] A. Morel, R. Grézaud, G. Pillonnet, P. Gasnier, G. Despesse, and A. Badel, "Active AC/DC control for wideband piezoelectric energy harvesting," *J. Phys., Conf. Ser.*, vol. 773, Nov. 2016, Art. no. 012059, doi: 10.1088/1742-6596/773/1/012059.

[21] A. Morel, A. Badel, R. Grézaud, P. Gasnier, G. Despesse, and G. Pillonnet, "Resistive and reactive loads' influences on highly coupled piezoelectric generators for wideband vibrations energy harvesting," *J. Intell. Mater. Syst. Struct.*, vol. 30, no. 3, pp. 386–399, Feb. 2019.

[22] A. Morel, R. Grézaud, G. Pillonnet, and A. Badel, "Piezoelectric generator frequency tuning and output power optimization through the use of an electronic interface," in *Proc. 11th Energy Harvesting Workshop*, Arlington, VA, USA, 2016.

[23] A. Brenes, A. Morel, J. Juillard, E. Lefeuvre, and A. Badel, "Maximum power point of piezoelectric energy harvesters: A review of optimality condition for electrical tuning," *Smart Mater. Struct.*, vol. 29, no. 3, Mar. 2020, Art. no. 033001, doi: 10.1088/1361-665X/ab6484.

[24] Y. Cai and Y. Manoli, "A piezoelectric energy-harvesting interface circuit with fully autonomous conjugate impedance matching, 156% extended bandwidth, and 0.38 μW power consumption," in *Proc. IEEE Int. Solid - State Circuits Conf.*, 2018, pp. 148–150, doi: 10.1109/ISSCC.2018.8310227.

[25] A. Morel et al., "32.2 Self-tunable phase-shifted SECE piezoelectric energy-harvesting IC with a 30nW MPPT achieving 446% energy-bandwidth improvement and 94% efficiency," in *Proc. IEEE Int. Solid-State Circuits Conf.*, 2020, pp. 488–490, doi: 10.1109/ISSCC19947.2020.9062972.

[26] L. Costanzo, A. L. Schiavo, and M. Vitelli, "Active interface for piezoelectric harvesters based on multi-variable maximum power point tracking," *IEEE Trans. Circuits Syst. I, Regular Papers*, vol. 67, no. 7, pp. 2503–2515, Jul. 2020, doi: 10.1109/TCSI.2020.2977495.

[27] S. Saggini, S. Giro, F. Ongaro, and P. Mattavelli, "Implementation of reactive and resistive load matching for optimal energy harvesting from piezoelectric generators," in *Proc. IEEE 12th Workshop Control Model. Power Electron.*, 2010, pp. 1–6, doi: 10.1109/COMPEL.2010.5562431.

[28] A. Morel, G. Pillonnet, D. Gibus, and A. Badel, "Discrete Optimal couple Tracking: A control scheme for electrical-tuning of strong coupling piezoelectric energy harvesters," *J. Intell. Mater. Syst. Structures*, vol. 34, pp. 785–799, 2022, Accessed: Jul. 06 2022. [Online]. Available: https://hal.archives-ouvertes.fr/hal-03680541

[29] Y. Huang, H.-C. Chen, P.-H. Hsieh, and Y.-C. Shu, "A calibration technique for P-SSHI-Phi interface for piezoelectric energy harvesting," in *Proc. IEEE Int. Symp. Circuits Syst.*, 2020, pp. 1–5, doi: 10.1109/ISCAS45731.2020.9180966.

[30] A. Badel and E. Lefeuvre, "Nonlinear conditioning circuits for piezoelectric energy harvesters," in *Nonlinearity in Energy Harvesting Systems*, E. Blokhina, A. El Aroudi, E. Alarcon, and D. Galayko, Eds., Cham, Switzerland: Springer, 2016, pp. 321–359, doi: 10.1007/978-3-319-20355-3_10.

[31] O. Freychet et al., "Efficient optimal load and maximum output power determination for linear vibration energy harvesters with a two-measurement characterization method," *Smart Mater. Struct.*, vol. 29, no. 1, Jan. 2020, Art. no. 015003, doi: 10.1088/1361-665X/ab516f.

[32] R. D'hulst, T. Sterken, R. Puers, G. Deconinck, and J. Driesen, "Power processing circuits for piezoelectric vibration-based energy harvesters," *IEEE Trans. Ind. Electron.*, vol. 57, no. 12, pp. 4170–4177, Dec. 2010, doi: 10.1109/TIE.2010.2044126.

[33] T. S. Paing and R. Zane, "Resistor emulation approach to low-power energy harvesting," in *Proc. 37th IEEE Power Electron. Specialists Conf.*, 2006, pp. 1–7, doi: 10.1109/pesc.2006.1711785.

[34] N. Kong and D. S. Ha, "Low-power design of a self-powered piezoelectric energy harvesting system with maximum power point tracking," *IEEE Trans. Power Electron.*, vol. 27, no. 5, pp. 2298–2308, May 2012, doi: 10.1109/TPEL.2011.2172960.

[35] N. Decroix, P. Gasnier, A. Morel, D. Gibus, and A. Badel, "Optimal impedance calculation with a two-measurement MPPT algorithm for piezoelectric vibration harvesters," in *Proc. 21st Int. Conf. Micro Nanotechnol. Power Gener. Energy Convers. Appl.*, Salt Lake City, UT, USA, 2022, pp. 62–65, doi: 10.1109/PowerMEMS56853.2022.10007581.

[36] S. Leadenham and A. Erturk, "Unified nonlinear electroelastic dynamics of a bimorph piezoelectric cantilever for energy harvesting, sensing, and actuation," *Nonlinear Dyn.*, vol. 79, no. 3, pp. 1727–1743, Feb. 2015, doi: 10.1007/s11071-014-1770-x.

[37] M. Shim, J. Kim, J. Jeong, S. Park, and C. Kim, "Self-powered 30 µw to 10 mW piezoelectric energy harvesting system with 9.09 ms/V maximum power point tracking time," *IEEE J. Solid-State Circuits*, vol. 50, no. 10, pp. 2367–2379, Oct. 2015, doi: 10.1109/JSSC.2015.2456880.

[38] L. Mamouri, T. Mesbahi, and V. Frick, "MPPT technique with improved FOCV control applied to a full active rectifier for low voltage piezoelectric energy harvesting," *IEEE Trans. Circuits Syst. II, Exp. Briefs*, vol. 71, no. 2, pp. 532–536, Feb. 2024, doi: 10.1109/TCSII.2023.3308956.

[39] X. Yue, S. Javvaji, Z. Tang, K. A. A. Makinwa, and S. Du, "A bias-flip rectifier with duty-cycle-based MPPT for piezoelectric energy harvesting," *IEEE J. Solid-State Circuits*, vol. 59, no. 6, pp. 1771–1781, Jun. 2024, doi: 10.1109/JSSC.2023.3313733.

[40] N. Rezaei-Hosseinabadi, A. Amoorezaei, A. Tabesh, S. A. Khajehoddin, R. Dehghani, and K. Moez, "A voltage feedback based maximum power point tracking technique for piezoelectric energy harvesting interface circuits," *IEEE Internet Things J.*, vol. 11, no. 11, pp. 20433–20442, Jun. 1, 2024, doi: 10.1109/JIOT.2024.3371191.

[41] Y. Liao and J. Liang, "Maximum power, optimal load, and impedance analysis of piezoelectric vibration energy harvesters," *Smart Mater. Struct.*, vol. 27, no. 7, Jul. 2018, Art. no. 075053, doi: 10.1088/1361-665X/aaca56.

[42] D. A. Sanchez, J. Leicht, E. Jodka, E. Fazel, and Y. Manoli, "21.2 A 4µW-to-1mW parallel-SSHI rectifier for piezoelectric energy harvesting of periodic and shock excitations with inductor sharing, cold start-up and up to 681% power extraction improvement," in *Proc. IEEE Int. Solid-State Circuits Conf.*, 2016, pp. 366–367, doi: 10.1109/ISSCC.2016.7418059.

[43] X. Wang et al., "A self-powered rectifier-less synchronized switch harvesting on inductor interface circuit for piezoelectric energy harvesting," *IEEE Trans. Power Electron.*, vol. 36, no. 8, pp. 9149–9159, Aug. 2021, doi: 10.1109/TPEL.2021.3052573.

[44] H. Xiao, H. Peng, H. Sun, Y. Zhao, X. Liu, and C. Jiang, "Automatic impedance matching with dual time-scale P&O in fully self-powered electromagnetic vibration energy harvesting," *IEEE Trans. Power Electron.*, vol. 39, no. 3, pp. 3377–3390, Mar. 2024, doi: 10.1109/TPEL.2023.3327458.

[45] K. Chen et al., "Self-sensed, self-adapted and self-powered piezoelectric generator architecture by synchronous circuits of autonomous parameter tuning," *Energy Convers. Manage.*, vol. 300, Jan. 2024, Art. no. 117919, doi: 10.1016/j.enconman.2023.117919.